Supplementary Information for "Manipulation of spin and magnetic anisotropy in bilayer magnetic molecular junctions"

Yu Wang,[1,2,3,*] Xiaoguang Li,[1,†] Xiao Zheng,[3] and Jinlong Yang[3]

[1] *Institute for Advanced Study, Shenzhen University, Shenzhen 518060, China*
[2] *Key Laboratory of Optoelectronic Devices and Systems of Ministry of Education and Guangdong Province, College of Optoelectronic Engineering, Shenzhen University, Shenzhen 518060, China*
[3] *Hefei National Laboratory for Physical Sciences at the Microscale and Synergetic Innovation Center of Quantum Information and Quantum Physics, University of Science and Technology of China, Hefei, Anhui 230026, China*

Here we provide the details of our methodology and some supplementary results. In Sec. S1 we introduce the details for computation of electronic structures and magnetic anisotropy. In Sec. S2 and Sec. S3 the Anderson impurity model (AIM) and HEOM approach for the theoretical study are presented. The comparison results of FePc/Pb(111) by using different exchange-correlation approximations are presented in Sec. S4. The electron occupation numerical analysis for the CoPc/FePc/Pb(111), FePc/CoPc/Pb(111) and FePc/FePc/Pb(111) composite systems are discussed in Sec. S5. The Fano and Frota fittings for the Kondo resonance in CoPc/FePc/Pb(111) are presented in Sec. S6. In Sec. S7 we verify the influence of the inter-orbital Coulomb repulsion U_{12} on the line shape of simulated dI/dV plots.

S1. Details for computation of electronic structures

From the point of view of delocalization error of density functional approximations (DFA),[1,2] the value of effective U is the deviation of the derivative gap from the fundamental (integer) gap.[3,4] It is important to note that the TM ions on different layers are subject to different chemical surroundings, and hence their local electronic and spin states are not equivalent. Therefore, they are expected to have different magnitudes of +U correction ($U_{\rm eff}$).[5] In the bilayer TMPc junction, the TMPc molecule in the second layer separated more than 3 Å from the substrate, is similar to a free case, and hence the +U correction on the TM d-orbitals can be considered as a local correction for the free one. For an isolated molecule, the integer gap is $E_{\rm gap}^{\rm int}$ =IP-EA, where IP is the ionization potential and EA is the electron affinity; and the derivative gap is the difference between the energy of highest occupied molecular orbital (HOMO) and that of lowest unoccupied molecular orbital (LUMO) $E_{\rm gap}^{\rm der} = \epsilon_{\rm LUMO} - \epsilon_{\rm HOMO}$. Our DFT calculations are: $E_{\rm gap}^{\rm int} = 3.647\,$eV, $E_{\rm gap}^{\rm der} = 1.539\,$eV, $U_{\rm eff} = E_{\rm gap}^{\rm int} - E_{\rm gap}^{\rm der}$ =2.1 eV for the CoPc molecule; $E_{\rm gap}^{\rm int} = 3.737\,$eV, $E_{\rm gap}^{\rm der} = 0.214\,$eV, $U_{\rm eff}$ =3.5 eV for the FePc molecule. Different approximations, namely local-density approximation (LDA),[6] generalized gradient approximation (GGA),[7] and GGA+van der Waals (vdW),[8] have been tested and the effect of different exchange-correlation approximations or the vdW interaction for the calculations is minimal. Therefore, $U_{\rm eff} = 2\,$eV and 3 eV are used for Co and Fe 3d electrons in the second layer. Since the first layer of TMPc superlattice serves as a spin-insulating buffer. Therefore, their Hubbard-like Coulomb and exchange parameters are set to the literature values for a singlet TMPc molecule, i.e., $U_{\rm eff} = 0$ in the first layer.

We adopt a hybrid approach to evaluate the MA of the FePc/CoPc/Pb(111) and FePc/FePc/Pb(111) composite junctions. For instance, the strength of axial MA is calculated via

$$D = D_{\rm FePc}^{\rm CASSCF} + (D_{\rm Ads\text{-}FePc}^{\rm DFT} - D_{\rm FePc}^{\rm DFT})\,. \qquad (1)$$

Here, $D_{\rm FePc}^{\rm CASSCF}$ is the axial MA of an isolated FePc molecule computed with the complete active space self-consistent field (CASSCF) method,[9–11] while $D_{\rm Ads\text{-}FePc}^{\rm DFT}$ and $D_{\rm FePc}^{\rm DFT}$ are the axial MAs of the composite system and an isolated FePc molecule calculated via DFT, respectively. The difference between the latter reflects the influence of the substrate environment.

In detail, the ground state of the FePc molecule is a triplet state with 6 electrons distributing on the five Fe d-orbitals. Thus, $D_{\rm FePc}^{\rm CASSCF}$ is obtained by CASSCF(6,5) calculations with the Douglas-Kroll-Hess relativistically recontracted def2-svp basis set[12,13] at the level of n-electron valence state perturbation theory (NEVPT2).[14] To speed up the calculations, the RIJCOSX approximation[15] (in combination with the def2-TZVP/C[16] auxiliary basis set) is used.

In the DFT calculation for MAE, a self-consistent calculation without the spin-orbital coupling is first performed to obtain the charge density of the ground state of the system. Using this charge density as input, the spin-orbital coupling (SOC) is treated as a perturbation in non-self-consistent calculations of two different magnetization directions. The MAE is defined as the total energy difference of the system as its different spin orientation. We obtain the values of D and E by using the following equations:[17]

$$D^{\rm DFT} = \epsilon_z - \frac{\epsilon_x + \epsilon_y}{2}\,, \quad E^{\rm DFT} = \epsilon_x - \epsilon_y\,, \qquad (2)$$

where $\epsilon_i\,(i = x, y, z)$ are the energy when the spin S

is aligned along the easy or hard axis z and the two transversal axes y and x.

The bilayer TMPc junction is modeled using $3\sqrt{3}\times 6$ supercells (18.19 Å×15 Å) with a slab thickness of ten layers and a 17.3 Å vacuum space in the z direction. Such a setup is considered reliable to obtained the accurate magnetic moment and MAE for the systems.[18] Each of the first-layer TMPc molecule adopts an on-top adsorption configuration, i.e., the TM ion sits right above a Pb atom, while the TM ions in the second layer reside right on top of those in the first layer, and the molecular plane is rotated by 45° around the normal axis.

In the DFT calculation, the SOC effect is not considered firstly during optimization, and all the atoms except those in the bottom five Pb layers are fully relaxed until the net force on every atom is smaller than 0.02 eV/Å. The convergence for the total energy is 10^{-5} eV (SOC calculation is 10^{-7} eV). Because of the large size of the supercell, structural optimizations adopt a Γ-centered $1\times 1\times 1\,k$ mesh only, while for electronic structure simulations, the SOC effect is considered and MAE is tested to converge at a k-point mesh of $3\times 3\times 1$. In our calculations a Gaussian smearing with a broadening of 0.05 eV is applied.

S2. Quantum impurity model

The total bilayer TMPc/Pb(111) composite system of interest is described by the following Anderson impurity model (AIM).[19] This model captures the characteristics of quantum transport system in which the correlated localized spins interact with the surrounding environment. we set $e=\hbar=1$ hereafter.

$$H_{\rm AIM}=H_{\rm imp}+H_{\rm env}+H_{\rm coup}\,. \tag{3}$$

Here, $H_{\rm imp}$ describes the magnetic impurities associated with the partially occupied TM d orbitals:

$$H_{\rm imp}=\sum_{\nu}\epsilon_{\nu}\hat{n}_{\nu}+U_{\nu}\sum_{\nu}\hat{n}_{\nu\uparrow}\hat{n}_{\nu\downarrow}+U_{\mu\nu}\sum_{\mu<\nu}\hat{n}_{\mu}\hat{n}_{\nu}+H_{\rm ZFS}\,. \tag{4}$$

Here, $\hat{n}_{\mu}=\sum_{\sigma}\hat{n}_{\mu\sigma}=\sum_{\sigma}\hat{d}^{\dagger}_{\mu\sigma}\hat{d}_{\mu\sigma}$ is the electron occupation number operator for the μth impurity orbital, with $\hat{d}^{\dagger}_{\mu\sigma}$ ($\hat{d}_{\mu\sigma}$) being the creation (annihilation) operator for a spin-σ ($\sigma=\uparrow$ or $\downarrow$) electron on the μth impurity orbital of energy $\epsilon_{\mu\sigma}$. $\{U_{\nu}\}$ and $\{U_{\mu\nu}\}$ represent the intra- and interorbital Coulomb repulsion, respectively.

The crystal-field splitting of the d levels together with the SOC give rise to the local MA effect, which is described by the effective spin Hamiltonian given by the last term $H_{\rm ZFS}$ in Eq. (4):[20,21]

$$H_{\rm ZFS}=DS_z^2+E(S_x^2-S_y^2)\,, \tag{5}$$

in which D and E represent the axial and in-plane anisotropy strengths, respectively. $\boldsymbol{S}=\{S_x,S_y,S_z\}$ is the impurity spin–S operator. The contribution of $H_{\rm ZFS}$ is equivalent to the magnetic anisotropy energy obtained via the DFT calculation, which is accounted for as the total energy difference when the spin moments align along different directions.[22–24]

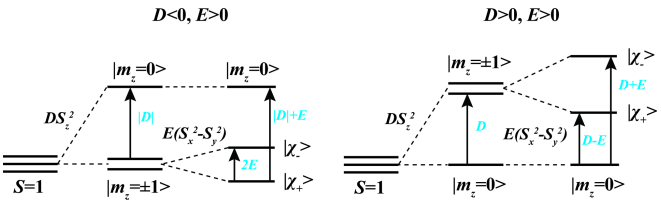

Figure S1. Schematic energy spectrum of adatom ground state multiplet for $S=1$ for uniaxial anisotropy D and finite in-plane anisotropy E.

According to previous studies,[25,26] the competition between MA and Kondo screening exhibits very characteristic features in the spectral function that can be measured directly by means of inelastic electron tunneling spectroscopy (IETS) using STM.[27] For instance, in the case of an integer impurity spin S system with finite uniaxial anisotropy $D\neq 0$ and in-plane anisotropy $E\neq 0$, the $(2S+1)$ degeneracy of the ground state multiplet is completely lifted. For $D>0$, the $|m_z=0\rangle$ state becomes the ground state and the $|m_z=\pm 1\rangle$ states become an excited doublet (taking $S=1$ as an example). A finite in-plane anisotropy $E>0$ allows for quantum tunneling between both spin directions thus lifting the degeneracy of the excited doublet, which becomes split by $2E$, leading to the bare excitation energies $\delta_1=D-E$ and $\delta_2=D+E$. The quantum states of the split doublet are thus linear combinations $|\chi_{\pm}\rangle\sim|m_z=+1\rangle\pm|m_z=-1\rangle$. This case suppresses the Kondo effect.[28] In contrast, for an integer impurity spin system with $D<0$, when $E=0$, the ground state is the doublet $|m_z=\pm 1\rangle$ and the state $|m_z=0\rangle$ is the first excited state. Further in-plane anisotropy term $E>0$ produces the quantum tunneling that leads to a splitting of the $|m_z=\pm 1\rangle$ doublet, so that the bare excitation energies are $\delta_1=2E$ and $\delta_2=|D|+E$; see Fig. S1. All the nonzero magnetic anisotropy D and E lead to spin-flip excitations from the ground states, which are signaled by steps in the dI/dV spectra at finite bias voltages corresponding to the excitation energies of the quantum magnet.[27]

The second term in Eq. (3) describes the conduction electron bath including the substrate and STM tip:

$$H_{\rm env}=H_{\rm tip}+H_{\rm sub}=\sum_{\alpha=t,s}\sum_{k\sigma}\epsilon_{\alpha k}\,\hat{c}^{\dagger}_{\alpha k\sigma}\hat{c}_{\alpha k\sigma}\,. \tag{6}$$

Here, $H_{\rm tip}$ and $H_{\rm sub}$ represent the STM tip ($\alpha=t$) and the Pb metal substrate ($\alpha=s$), respectively. $\hat{c}^{\dagger}_{\alpha k\sigma}$ ($\hat{c}_{\alpha k\sigma}$) is the creation (annihilation) operator for a spin–σ electron on the single-electron state $|k\rangle$ of energy $\epsilon_{\alpha k}$. Note that $H_{\rm sub}$ of Eq. (6) does not include the superconducting states in the Pb substrate that would emerge below

the critical temperature of 7.2 K. This is because in the related STM experiments the superconducting states are completely quenched by a finite magnetic field.[29,30] It would be interesting to investigate the influence of superconducting states on the Kondo phenomena,[31–34] which is however beyond the scope of the present work. Finally, the third term in Eq. (3) is the so-called hybridization term, which describes the coupling between the impurity and the environment:

$$H_{\rm coup} = \sum_{\alpha k\nu}\sum_{\sigma} V_{\alpha k\nu}\, \hat{c}^{\dagger}_{\alpha k\sigma}\hat{d}_{\nu\sigma} + {\rm H.c.} \tag{7}$$

Here, $V_{\alpha k\nu}$ is the coupling strength between the νth impurity orbital and the reservoir state $|k\rangle$. In this work, we only consider nonzero $V_{\alpha k\nu}$ between TM d orbitals and reservoirs states. This corresponds to the experimental situation that the STM tip is placed on top of a TM center.[29] It is possible to study the situation that the STM tip is positioned above some other spots of the TMPc molecule (such as on top of a coordinating ligand), and hence acquire a certain level of spatial resolution in the measurement. Regarding the theoretical model, it is then necessary to include some orbitals of the coordinating ligands into the impurity.[35–39] Furthermore, the direct coupling between the STM tip and the Pb substrate is not included in our model, because such a coupling is supposedly rather weak due to the large tip-substrate distance.[40] The influence of reservoir environment on the impurities is accounted for through the hybridization functions, which are defined by $\Gamma_{\alpha\nu}(\omega) \equiv \pi\sum_k |V_{\alpha k\nu}|^2\, \delta(\omega-\epsilon_{\alpha k})$. For numerical convenience, we adopt a Lorentzian form of $\Gamma_{\alpha\nu}(\omega) = \frac{\Delta_\alpha}{2}\frac{W_\alpha^2}{(\omega-\Omega_\alpha)^2+W_\alpha^2}$, where W_α is the bandwidth of the tip or the substrate, Ω_α is the band center that is aligned with the reservoir chemical potential, and Δ_α is the effective impurity-reservoir coupling strength. In relation to the STM experiments, the tip-impurity coupling assumes a small value ($\Delta_t \ll \Delta_s$) because of their large separation. The weak tip-impurity hybridization suggests that the tip states have rather minor influence on the Kondo resonance.[41] Nevertheless, the tip enables a direct measurement of electric current through the composite system, and is thus explicitly included in the AIM. It is emphasized that all the involving parameters of the AIM are to be determined from the DFT calculations,[42–44] and hence our quantum impurity model is constructed based on first principles.

- $\epsilon_i = \int_{-\infty}^{0}\rho_i(\omega)\,\omega\,d\omega \big/ \int_{-\infty}^{0}\rho_i(\omega)\,d\omega$ is estimated as the energy difference between the center of the occupied ith d-band and the equilibrium chemical potential $\mu^{\rm eq}$. Here, $\rho_i(\omega)$ is the PDOS of the ith d-orbital, and we have set $\mu^{\rm eq}=0$.
- $n_i = \int_{-\infty}^{0}\rho_i(\omega)\,d\omega$.
- Δ_{si} is estimated as the change in $\rho_i(\omega)$ distribution width in the absence of the substrate; and Δ_{ti} is chosen to be one order of magnitude smaller than Δ_{si} to mimic the experimental situation.
- W_α is estimated as the width of the energy bands of the substrate or the STM tip which have nonzero coupling to the impurity d-orbitals.
- U_i is estimated as the energy difference between the centers of the ith occupied spin-up and unoccupied spin-down d-bands.

S3. HEOM approach

The parameterized AIM of Eq. (3) is then solved with the HEOM approach,[45–47] as described in more detail in previous works.[42–44] The final HEOM are cast into a compact form of

$$\begin{aligned}\dot{\rho}^{(n)}_{j_1\cdots j_n} =& -\left(i\mathcal{L}+\sum_{r=1}^{n}\gamma_{j_r}\right)\rho^{(n)}_{j_1\cdots j_n} - i\sum_j \mathcal{A}_{\bar{j}}\,\rho^{(n+1)}_{j_1\cdots j_n j}\\ & - i\sum_{r=1}^{n}(-)^{n-r}\mathcal{C}_{j_r}\rho^{(n-1)}_{j_1\cdots j_{r-1}j_{r+1}\cdots j_n}\,.\end{aligned} \tag{8}$$

Here, $\mathcal{L}\star = [H_{\rm imp},\star]$ is the Liouvillian of the impurity, and $\mathcal{A}_{\bar{j}}$ and $\mathcal{C}_{j_r}$ are Grassmann superoperators, whose detailed forms have been presented in Ref. 45. The HEOM approach consists of a series of basic variables, namely the reduced system density matrix $\rho^{(0)}(t) = {\rm tr}_{\rm env}\,\rho_{\rm total}(t)$ and the auxiliary density operators $\{\rho^{(n)}_{j_1\cdots j_n}(t); n=1,\ldots,L\}$, with $j\equiv(\varsigma\nu\alpha m)$ being a multi-component index and L denoting the truncation level for the hierarchy. With the HEOM approach, in principle the exact solution is achieved at $L\to\infty$. In practice the results usually converge rapidly and uniformly with the increasing L. Once convergence is reached at a certain L, the numerical outcome is guaranteed to be quantitatively accurate.[46] With the limited computational resources at our disposal, in this work the $L=4$ truncation is adopted unless otherwise specified, and we have verified that the numerical results are reasonably accurate.

For the AIM system described by Eq. (3), the electric current flowing into the αth lead is defined by

$$I_\alpha(t) \equiv -\frac{d\langle\hat{N}_\alpha\rangle}{dt} = i\left\langle\left[\hat{N}_\alpha, H_{\rm AIM}\right]\right\rangle_{\rm total}. \tag{9}$$

Here, $\langle\star\rangle_{\rm total}\equiv {\rm tr}_{\rm total}[\star\,\rho_{\rm total}(t)]$ with ${\rm tr}_{\rm total}\equiv{\rm tr}_{\rm imp}{\rm tr}_{\rm env}$. $\hat{N}_\alpha$ is the electron occupation number operator for the αth lead, which satisfies $[\hat{N}_\alpha, H_{\rm imp}] = [\hat{N}_\alpha, H_{\rm env}] = 0$. In the HEOM formalism, the remaining commutator $[\hat{N}_\alpha, H_{\rm coup}]$ that contributes nontrivially to the current is directly related to the first-tier auxiliary density matrices $\{\rho^{(1)}_j(t)\}$; see Eq. (3.14) of Ref. 45 for details. Therefore, in the framework of HEOM, the electric current is evaluated via

$$I_\alpha(t) = -2\,{\rm Im}\sum_{i\sigma m}{\rm tr}_{\rm imp}\left(\hat{d}_{i\sigma}\,\rho^{(1)}_j\right)_{\varsigma=+}. \tag{10}$$

Table S1. Computed the distance $d_{\mathrm{Fe-Pb}}$ (in unit of Å) between the Fe ion and the Pb atom below and electronic magnetic moment (in unit of μ_B) for the FePc/Pb(111) composite, obtained within different DFT approximations.

	GGA	GGA+vdW	LDA
$d_{\mathrm{Fe-Pb}}$	2.76	2.74	2.64
Magnetic moment	0.61	0.34	0.00

At stationary states (equilibrium state or nonequilibrium steady state), the HEOM (8) become a set of coupled linear equations. The steady-state tunneling current in an STM experiment[48] ($I = |I_t^{\mathrm{st}}| = |I_s^{\mathrm{st}}|$) is calculated by using Eq. (10). The differential conductance dI/dV is then obtained with a finite difference analysis.

Another important dynamical property of the impurity is the spectral density function which could be measured experimentally via the angle-resolved photoemission spectroscopy.[49] In the framework of HEOM, the spectral density function of the impurity at a stationary state can be calculated based on a linear response theory established in the HEOM Liouville space.[46] For the ith impurity orbital in the AIM, the spin-σ spectral density function $A_{i\sigma}(\omega)$ is evaluated via

$$\begin{aligned} A_{i\sigma}(\omega) &\equiv \frac{1}{2\pi}\int dt\, e^{i\omega t}\left\langle\left\{\hat{d}_{i\sigma}(t), \hat{d}_{i\sigma}^{\dagger}(0)\right\}\right\rangle \\ &= \frac{1+e^{-\omega/k_BT}}{2\pi}\int dt\, e^{i\omega t}\left\langle \hat{d}_{i\sigma}(t)\, \hat{d}_{i\sigma}^{\dagger}(0)\right\rangle, \quad (11) \end{aligned}$$

and $A_i(\omega) = \sum_\sigma A_{i\sigma}(\omega)$.

S4. Ground state of FePc/Pb(111)

The DFT calculations yield the optimized adsorption conformations and electronic structures of the FePc/Pb(111) composite as depicted in Fig. S2. As reported in previous studies,[37,50–52] the electronic structures of TMPc/metal composite systems (TM=Co, Fe) are sensitive to the choice of the exchange-correlation functional, i.e., LDA, GGA and the presence or absence of the vdW correction. In the following, the influence of the different exchange-correlation functionals on the structural and magnetic electronic properties of the FePc/Pb(111) composite is thoroughly analyzed.

Table S1 summarizes the variation in the distance $d_{\mathrm{Fe-Pb}}$ between the Fe ion and the Pb atom below and electronic magnetic moment for the FePc/Pb(111) composite with the change of the exchange-correlation functionals. The computed distance $d_{\mathrm{Fe-Pb}}$ between the Fe ion and the Pb atom below with LDA is ~ 2.64 Å, which is known to be underestimated.[37] In contrast, the result with GGA shows that $d_{\mathrm{Fe-Pb}}$ increases to ~ 2.76 Å. While by using GGA+vdW, i.e., by switching on the vdW interaction, the distance $d_{\mathrm{Fe-Pb}}$ is ~ 2.74 Å. Here, we note that the values of $d_{\mathrm{Fe-Pb}}$ obtained with GGA and GGA+vdW are quite similar, in contrast to the case of TMPc molecules adsorbed on the Ag(100) surface,[37] where the GGA+vdW method leads to a shorter distance between the adsorbed molecule and the surface.[50,53] This is because the more-reactive Pb(111) surface.[54] Meanwhile, the optimized molecular conformation with three exchange-correlation functionals exhibits similar result. Clearly, the FePc molecules become slightly convex after deposition, with its periphery slightly away from the surface. The molecules absorption also induces a small distortion of the substrate, pulling the Pb atom below Fe ion slightly upper than the surface plane: see the upper panel of Fig. S2.

Accordingly, various $d_{\mathrm{Fe-Pb}}$ indicates the interactions between the adsorbed molecule and the substrate are different, which is expected to have nontrivial influences on their electronic structures. Calculations for the spin-polarized PDOS of the FePc molecule in the FePc/Pb(111) composite within different DFT approximations confirm the conclusion, as depicted in the lower panel of Fig. S2. The Fermi level E_F is set as zero energy hereafter. Interestingly, the PDOS of majority-spin (↑) and minority-spin (↓) states by using GGA within the current energy window are mostly symmetric distributed except the d states of the Fe ion, where the minority-spin PDOS is shifted right about 0.8 eV compared to the majority-spin PDOS. Such PDOS distributions lead to a small overall magnetic moment of $\sim 0.61\,\mu_B$. Similar behavior is also found in the PDOS distribution within GGA+vdW method, which has a value of $\sim 0.34\,\mu_B$. However, the LDA-calculated PDOS of majority-spin and minority-spin states are nearly identical, leading to the almost zero total magnetic moment.

According to the above DFT calculations, the spins at the metal centers of the FePc molecule undergo partial or total quenching, which is also observed in similar TMPc/metal adsorption systems.[21,55–57] In contrast to the molecular spin $S = 1$ state in the freestanding FePc molecule or the FePc/Au(111) adsorption system,[43,58,59] the FePc/Pb(111) composite is considered to be in a nonmagnetic local $S = 0$ state, analogous to the case of monolayer CoPc on the Pb(111).[29,30] Such a difference is closely related to the coupling of the FePc molecule with the different substrate. As depicted in the lower panel of Fig. S2, the large density of states near the Fermi level E_F indicates a strong coupling of FePc with the substrate,[43,59] and the charge transfer between them results in the spin conversion from $S = 1$ to $S = 0$. Note that the measured dI/dV spectra show neither the Zeeman splitting nor the Kondo resonance for the monolayer FePc on metallic substrate,[60,61] which suggest that the magnetic moment of the FePc monolayer is completely quenched by the couplings between the FePc molecules and the substrate. Therefore, only the LDA exchange-correlation functional gives the nonmagnetic local $S = 0$ state coinciding with the experiments. Unless otherwise stated, the results presented in the next sections are obtained using the LDA

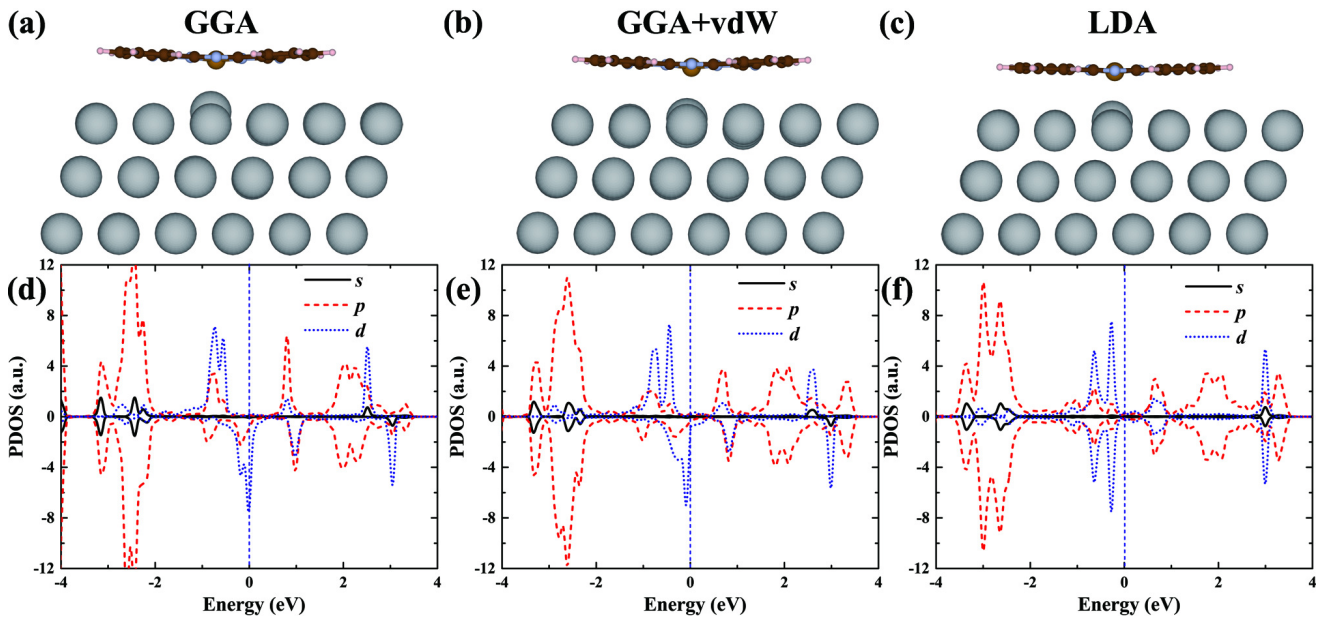

Figure S2. The optimized geometric structures and calculated spin-resolved PDOS of the FePc molecule in the FePc/Pb(111) composite by using different DFT approximations, namely GGA+vdW, GGA and LDA. The blue vertical dash lines in the lower panel indicate the Fermi energy E_F that is set to zero. The ten-layer Pb substrate is simplified to a three-layer one for a clear comparison hereafter.

Table S2. Electron occupation numbers for the five d orbital of Fe and Co ions in the bilayer CoPc/FePc/Pb(111) composite. Here, $n_{\rm occ} = n_\uparrow + n_\downarrow$ and $S_z = \frac{1}{2}(n_\uparrow - n_\downarrow)$, with $n_\uparrow$ and $n_\downarrow$ being the spin-up and spin-down occupation numbers, respectively.

Fe	d_{xy}	d_{yz}	d_{z^2}	d_{xz}	$d_{x^2-y^2}$	Total
$n_\uparrow$	0.407	0.651	0.659	0.647	0.904	3.268
$n_\downarrow$	0.405	0.633	0.633	0.631	0.903	3.205
$n_{\rm occ}$	0.812	1.284	1.292	1.278	1.807	6.473
S_z	0.001	0.009	0.013	0.008	0.000	0.031
Co	d_{xy}	d_{yz}	d_{z^2}	d_{xz}	$d_{x^2-y^2}$	Total
$n_\uparrow$	0.947	0.911	0.926	0.911	0.446	4.141
$n_\downarrow$	0.938	0.880	0.152	0.879	0.403	3.252
$n_{\rm occ}$	1.885	1.791	1.077	1.790	0.849	7.393
S_z	0.004	0.016	0.386	0.016	0.021	0.445

exchange-correlation functional.

S5. Electron occupation analyze

The electron occupation number on each of the TM d orbitals for both layers are analyzed and listed in Tables S2 and S3, along with their contributions to the local magnetic moment. The occupation number is evaluated via $n_{i\sigma} = \int_{-\infty}^{E_F} \rho_{i\sigma}(\omega)\, d\omega$, with $\rho_{i\sigma}(\omega)$ being the spin–σ PDOS of ith d orbital.

Table S3. Electron occupation numbers for the five d orbitals of TM ions in the two FePc/CoPc/Pb(111) and FePc/FePc/Pb(111) composites. The same convention is adopt as in Table S2.

Co	d_{xy}	d_{yz}	d_{z^2}	d_{xz}	$d_{x^2-y^2}$	Total
$n_\uparrow$	0.442	0.804	0.743	0.785	0.923	3.697
$n_\downarrow$	0.442	0.792	0.765	0.787	0.923	3.709
$n_{\rm occ}$	0.884	1.596	1.508	1.572	1.846	7.406
S_z	0.000	0.006	-0.011	-0.001	0.000	-0.006
Fe	d_{xy}	d_{yz}	d_{z^2}	d_{xz}	$d_{x^2-y^2}$	Total
$n_\uparrow$	0.938	0.929	0.918	0.903	0.433	4.121
$n_\downarrow$	0.929	0.084	0.097	0.728	0.356	2.194
$n_{\rm occ}$	1.867	1.013	1.015	1.631	0.789	6.315
S_z	0.004	0.423	0.410	0.087	0.038	0.963
Fe	d_{xy}	d_{yz}	d_{z^2}	d_{xz}	$d_{x^2-y^2}$	Total
$n_\uparrow$	0.406	0.641	0.657	0.639	0.906	3.249
$n_\downarrow$	0.405	0.631	0.647	0.630	0.905	3.218
$n_{\rm occ}$	0.811	1.272	1.304	1.269	1.811	6.467
S_z	0.000	0.005	0.005	0.004	0.000	0.015
Fe	d_{xy}	d_{yz}	d_{z^2}	d_{xz}	$d_{x^2-y^2}$	Total
$n_\uparrow$	0.950	0.911	0.921	0.911	0.483	4.176
$n_\downarrow$	0.050	0.792	0.091	0.791	0.390	2.114
$n_{\rm occ}$	1.000	1.703	1.012	1.702	0.873	6.280
S_z	0.450	0.060	0.415	0.060	0.047	1.031

S6. Fano and Frota Fitting

In the manuscript, the fitting of the Kondo resonance is performed with a Frota function. However, in some cases,

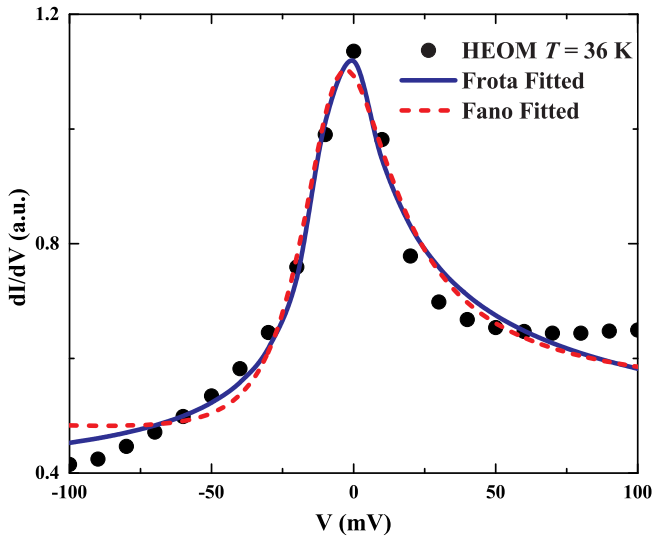

Figure S3. The solid and short dashed curves correspond to the best fits using a Frota and Fano function for the HEOM calculation results at $T = 36$ K. The resulting fit parameters for the Fano and Frota curves are: $q = -0.245$, $\epsilon_0 = -7.457$ meV, and $\Gamma = 19.486$ meV; $\phi = -23.447$, $\omega_0 = -5.959$ meV, and $\Gamma_F = 9.559$ meV.

a better fit to the experimental data may be realized using a Fano function,[62,63] which is described by the following expression:

$$\frac{dI}{dV} \simeq a\frac{(\epsilon + q)^2}{1 + \epsilon^2} + b \tag{12}$$

with the energy-dependent variable $\epsilon = V - \epsilon_0/\Gamma$, the asymmetry parameter q, constants a and b, the energy position of the resonance ϵ_0, and the half-width at half maximum (HWHM) of Γ. In Fig. S3, we show both Fano and Frota fits to the Kondo peak in the calculated dI/dV spectra at $T = 36$ K. In the low-bias regime, the resonance features are well-described by both fits. However, as V increases only the Frota fit yields a better approximation for the dI/dV plot than the Fano function.

S7. The influence of U_{12} on simulated dI/dV plot

As depicted in Fig. S4, we carry out additional tests and verify that reasonable inter-orbital Coulomb repulsion $U_{12} < U_1(U_2)$ has no significant difference in the typical step features of simulated dI/dV plots by using a simplified two-orbital AIM.

* yuwang@mail.ustc.edu.cn
† xgli@szu.edu.cn

[1] A. J. Cohen, P. Mori-Sánchez, and W. Yang, Science **321**, 792 (2008).
[2] A. J. Cohen, P. Mori-Sánchez, and W. Yang, Chem. Rev **112**, 289 (2012).
[3] X. Zheng, A. J. Cohen, P. Mori-Sánchez, X. Hu, and W. Yang, Phys. Rev. Lett. **107**, 026403 (2011).
[4] A. J. Cohen, P. Mori-Sánchez, and W. Yang, Phys. Rev. B **77**, 115123 (2008).
[5] M. Cococcioni and S. De Gironcoli, Phys. Rev. B **71**, 035105 (2005).
[6] J. P. Perdew and A. Zunger, Phys. Rev. B **23**, 5048 (1981).
[7] J. P. Perdew, K. Burke, and M. Ernzerhof, Phys. Rev. Lett. **77**, 3865 (1996).
[8] S. Grimme, J. Antony, S. Ehrlich, and H. Krieg, J. Chem. Phys. **132**, 154104 (2010).
[9] B. O. Roos, Int. J. Quantum Chem. **18**, 175 (1980).
[10] F. Neese, J. Chem. Phys. **127**, 164112 (2007).
[11] F. Neese, J. Am. Chem. Soc. **128**, 10213 (2006).
[12] B. Sandhoefer and F. Neese, J. Chem. Phys. **137**, 094102 (2012).
[13] F. Weigend, Phys. Chem. Chem. Phys. **8**, 1057 (2006).
[14] C. Angeli, R. Cimiraglia, S. Evangelisti, T. Leininger, and J.-P. Malrieu, J. Chem. Phys. **114**, 10252 (2001).
[15] F. Weigend and R. Ahlrichs, Phys. Chem. Chem. Phys. **7**, 3297 (2005).
[16] A. Hellweg, C. Hättig, S. Höfener, and W. Klopper, Theor. Chem. Acc. **117**, 587 (2007).
[17] D.-J. Choi, R. Robles, J.-P. Gauyacq, M. Ternes, S. Loth, and N. Lorente, Phys. Rev. B **94**, 085406 (2016).
[18] O. Šipr, S. Bornemann, J. Minár, and H. Ebert, Phys. Rev. B **82**, 174414 (2010).
[19] P. W. Anderson, Phys. Rev. **124**, 41 (1961).
[20] D. Gatteschi, R. Sessoli, and J. Villain, *Molecular nanomagnets*, Oxford University Press, Oxford, 2006.
[21] N. Tsukahara, K.-i. Noto, M. Ohara, S. Shiraki, N. Takagi, Y. Takata, J. Miyawaki, M. Taguchi, A. Chainani, S. Shin, and M. Kawai, Phys. Rev. Lett. **102**, 167203 (2009).
[22] D. S. Wang, R. Wu, and A. J. Freeman, Phys. Rev. B **47**, 14932 (1993).
[23] X. Wang, D. S. Wang, W. Ruqian, and A. J. Freeman, J. Magn. Magn. Mater. **159**, 337 (1996).
[24] B. S. Yang, J. Zhang, L. N. Jiang, W. Z. Chen, P. Tang, X.-G. Zhang, Y. Yan, and X. F. Han, Phys. Rev. B **95**, 174424 (2017).
[25] D. Jacob and J. Fernández-Rossier, Eur. Phys. J. B **89**, 210 (2016).
[26] D. Jacob, Phys. Rev. B **97**, 075428 (2018).
[27] C. F. Hirjibehedin, C.-Y. Lin, A. F. Otte, M. Ternes, C. P. Lutz, B. A. Jones, and A. J. Heinrich, Science **317**, 1199 (2007).
[28] R. Žitko, R. Peters, and T. Pruschke, Phys. Rev. B **78**, 224404 (2008).
[29] X. Chen, Y.-S. Fu, S.-H. Ji, T. Zhang, P. Cheng, X.-C. Ma, X.-L. Zou, W.-H. Duan, J.-F. Jia, and Q.-K. Xue, Phys. Rev. Lett. **101**, 197208 (2008).
[30] Y.-S. Fu, T. Zhang, S.-H. Ji, X. Chen, X.-C. Ma, J.-F. Jia, and Q.-K. Xue, Phys. Rev. Lett. **103**, 257202 (2009).
[31] A. Yazdani, B. A. Jones, C. P. Lutz, M. F. Crommie, and D. M. Eigler, Science **275**, 1767 (1997).

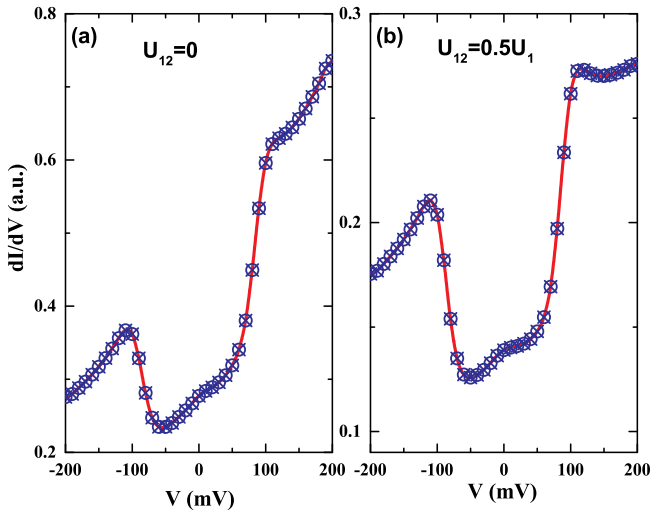

Figure S4. Calculated dI/dV plots for the two-orbital AIM corresponding to the FePc/FePc/Pb(111) composite at $T = 60\,K$ adopting various values of (a) $U_{12} = 0$, (a) $U_{12} = 0.5U_1$. The parameters are (in units of eV) $\epsilon_1 = -4.49$, $U_1 = 5.08$, $\epsilon_2 = -3.58$, $U_2 = 5.01$, $\Delta_1 = 0.09$, $\Delta_2 = 0.15$, $\bar{D}_2 = -0.112$, $\bar{E}_2 = 0.0$, $W_t = 5.5$ and $W_s = 5.85$.

[32] K. J. Franke, G. Schulze, and J. I. Pascual, Science **332**, 940 (2011).

[33] J. Bauer, J. I. Pascual, and K. J. Franke, Phys. Rev. B **87**, 075125 (2013).

[34] B. W. Heinrich, L. Braun, J. I. Pascual, and K. J. Franke, Nano Lett. **15**, 4024 (2015).

[35] U. G. E. Perera, H. J. Kulik, V. Iancu, L. G. G. V. Dias da Silva, S. E. Ulloa, N. Marzari, and S.-W. Hla, Phys. Rev. Lett. **105**, 106601 (2010).

[36] A. Mugarza, C. Krull, R. Robles, S. Stepanow, G. Ceballos, and P. Gambardella, Nat. Commun. **2**, 490 (2011).

[37] A. Mugarza, R. Robles, C. Krull, R. Korytár, N. Lorente, and P. Gambardella, Phys. Rev. B **85**, 155437 (2012).

[38] E. Minamitani, Y.-S. Fu, Q.-K. Xue, Y. Kim, and S. Watanabe, Phys. Rev. B **92**, 075144 (2015).

[39] J. Meyer, R. Ohmann, A. Nickel, C. Toher, R. Gresser, K. Leo, D. A. Ryndyk, F. Moresco, and G. Cuniberti, Physical Review B **93**, 155118 (2016).

[40] G. Chiappe and E. Louis, Phys. Rev. Lett. **97**, 076806 (2006).

[41] M. Misiorny, I. Weymann, and J. Barnaś, Phys. Rev. B **86**, 245415 (2012).

[42] Y. Wang, X. Zheng, B. Li, and J. Yang, J. Chem. Phys. **141**, 084713 (2014).

[43] Y. Wang, X. Zheng, and J. Yang, Phys. Rev. B **93**, 125114 (2016).

[44] Y. Wang, X. Zheng, and J. Yang, J. Chem. Phys. **145**, 154301 (2016).

[45] J. Jin, X. Zheng, and Y. Yan, J. Chem. Phys. **128**, 234703 (2008).

[46] Z. Li, N. Tong, X. Zheng, D. Hou, J. Wei, J. Hu, and Y. Yan, Phys. Rev. Lett. **109**, 266403 (2012).

[47] S. Wang, X. Zheng, J. Jin, and Y. Yan, Phys. Rev. B **88**, 035129 (2013).

[48] O. Y. Kolesnychenko, G. M. M. Heijnen, A. K. Zhuravlev, R. de Kort, M. I. Katsnelson, A. I. Lichtenstein, and H. van Kempen, Phys. Rev. B **72**, 085456 (2005).

[49] A. Damascelli, Z. Hussain, and Z.-X. Shen, Rev. Mod. Phys. **75**, 473 (2003).

[50] J. Brede, N. Atodiresei, S. Kuck, P. Lazić, V. Caciuc, Y. Morikawa, G. Hoffmann, S. Blügel, and R. Wiesendanger, Phys. Rev. Lett. **105**, 047204 (2010).

[51] E. Minamitani, N. Takagi, and S. Watanabe, Phys. Rev. B **94**, 205402 (2016).

[52] I. E. Brumboiu, S. Haldar, J. Lüder, O. Eriksson, H. C. Herper, B. Brena, and B. Sanyal, J. Chem. Theory Comput. **12**, 1772 (2016).

[53] M. Rosa, S. Corni, and R. Di Felice, Phys. Rev. B **90**, 125448 (2014).

[54] Y. H. Jiang, W. D. Xiao, L. W. Liu, L. Z. Zhang, J. C. Lian, K. Yang, S. X. Du, and H.-J. Gao, J. Phys. Chem. C **115**, 21750 (2011).

[55] A. Zhao, Q. Li, L. Chen, H. Xiang, W. Wang, S. Pan, B. Wang, X. Xiao, J. Yang, J. G. Hou, and Q. Zhu, Science **309**, 1542 (2005).

[56] M. Schmid, A. Kaftan, H.-P. Steinrück, and J. M. Gottfried, Surf. Sci. **606**, 945 (2012).

[57] P. Gargiani, G. Rossi, R. Biagi, V. Corradini, M. Pedio, S. Fortuna, A. Calzolari, S. Fabris, J. C. Cezar, N. B. Brookes, and M. G. Betti, Phys. Rev. B **87**, 165407 (2013).

[58] E. Minamitani, N. Tsukahara, D. Matsunaka, Y. Kim, N. Takagi, and M. Kawai, Phys. Rev. Lett. **109**, 086602 (2012).

[59] Y. Wang, X. Li, X. Zheng, and J. Yang, J. Chem. Phys. **147**, 134701 (2017).

[60] X. Liu, *Spin Excitation and Spin Polarization Study of Magnetic Molecules and Magnetic Nanostructures on Metal Surfaces*, PhD thesis, University of Science and Technology of China, 2012.

[61] N. Ohta, R. Arafune, N. Tsukahara, M. Kawai, and N. Takagi, J. Phys. Chem. C **117**, 21832 (2013).

[62] J. Li, W.-D. Schneider, R. Berndt, and B. Delley, Phys. Rev. Lett. **80**, 2893 (1998).

[63] V. Madhavan, W. Chen, T. Jamneala, M. F. Crommie, and N. S. Wingreen, Science **280**, 567 (1998).